RSC Advances

PAPER

View Article Online
View Journal | View Issue

Cite this: *RSC Adv.*, 2023, **13**, 30101

Intrinsically dominated anomalous Hall effect in pulsed laser deposited epitaxial Co_2MnGe ferromagnetic full Heusler alloy thin films†

Ekta Yadav and Sunil Kumar *

Received 8th September 2023
Accepted 10th October 2023

DOI: 10.1039/d3ra06132a

rsc.li/rsc-advances

Large size epitaxial thin films of ferromagnetic Co_2MnGe full Heusler alloy are grown over MgO(100) substrate by using pulsed laser deposition technique under optimized growth conditions. Metallic behavior is confirmed from the longitudinal resistivity-temperature data, while a minimum in the resistivity at ~25 K is attributed to the disorder-induced weak localization effect. Importantly, a dominating intrinsic anomalous Hall conductivity value of ~21 S cm^{-1} against an overall anomalous Hall conductivity value of ~36 S cm^{-1} at the room temperature has been estimated for the epitaxial Co_2MnGe film. The dominating intrinsic mechanism is also evident from the near temperature-independent behavior of the overall anomalous Hall conductivity.

1. Introduction

Search for novel materials with potential for advanced technological applications has always been driving the research efforts by material scientists and engineers. Heusler alloys are one of the important breakthrough materials which were discovered for the first time in year 1903,[1] since when the number of possible compositions having physical properties spanning multiple fields of the material science has enormously grown. Every time, new observations in one or more of their types, for example, the half-metallicity,[2] nontrivial topological states,[3] superconductivity,[4] have been regenerating the interest in these systems. Co-based ferromagnetic full Heusler alloys are quite interesting systems due to their remarkable characteristics, including the high Curie temperature (T_c), and tunable electronic and magnetic properties.[5–7] They possess unique half-metallic property wherein bands of one type spin exhibit metallic nature while the bands of the other are semiconducting or insulating.[2,8] Among the possible Co-based ferromagnetic full Heusler alloys, the ternary Co_2MnGe has been shown, both theoretically and experimentally, to exhibit half-metallicity[2,9,10] along with high Curie temperature, $T_c \sim 905$ K (ref. 11) and large saturation magnetization, $M_s \sim 5\mu_B$ f.u.$^{-1}$.[12] Such properties deem it to be fit for use in spintronic devices, for example, magnetic electrodes in magnetic tunnel junctions[13] and magnetic memory devices.[10,14,15] The possibility of Co_2MnGe as being a Weyl semimetal is strengthened from a recent theoretical study on a clean Co_2MnGe system[16] and another experimental study using angle-resolved photoemission spectroscopy (ARPES) on Co_2MnGe single crystal,[9] where two topological cones near the Fermi level could be located. The presence of Berry curvature in the topological non-trivial band structure of a material system is expected to give rise to several unique transport phenomena, including the large anomalous Hall effect (AHE) and chiral anomaly effect.[9,17–19]

In the Hall measurements, AHE manifests itself as an additional contribution in the developed transverse voltage. Fundamentally, the interaction between a spontaneous magnetization (M) and spin–orbit coupling (SOC) in the system is the origin for AHE,[20–22] where extrinsic and intrinsic mechanisms are involved. The extrinsic contribution to AHE arises from asymmetric scattering events, such as skew scattering and side jumps, from defects/disorders. On the other hand, the intrinsic mechanism elucidates the role of SOC in the electronic band structure of the ferromagnetic metal. The Karplus and Luttinger theory (KL theory) in terms of Berry phase[20,21,23,24] is popularly used to analyze the intrinsic behavior of the AHE. To distinguish between the intrinsic and extrinsic mechanisms contributing to the AHE, experimentally measured anomalous Hall resistivity is analyzed by certain scaling relation with the longitudinal resistivity.[19,25,26] While many studies in the literature have explored AHE in Co-based Heusler alloys,[3,27–29] there exists only one such study on the Co_2MnGe system, where Obaida *et al.*[30] reported AHE in polycrystalline Co_2MnGe thin film grown by sputtering. It was inferred from those results that AHE is predominantly influenced by extrinsic scattering, specifically, the skew scattering in the sample. More such studies on the other forms, *viz.*, the epitaxial films and single crystals of Co_2MnGe are highly desirable.

Department of Physics, Indian Institute of Technology Delhi, New Delhi 110016, India. E-mail: kumarsunil@physics.iitd.ac.in

† Electronic supplementary information (ESI) available. See DOI: https://doi.org/10.1039/d3ra06132a

In the present study, we report intrinsically dominated AHE in epitaxial Co_2MnGe thin films grown on MgO(100) substrate by pulsed laser deposition (PLD) technique under optimized growth conditions. While the epitaxial growth of the Co_2MnGe thin films were previously reported using molecular beam epitaxy (MBE)[12] and sputtering techniques,[31,32] however, the same by using PLD technique on MgO substrate are lacking. Structural properties were investigated by X-ray diffraction and ϕ-scan measurements to establish the epitaxial nature of the films. The dominating intrinsic AHE in the films is established by fitting the experimental results from magnetotransport measurements with appropriate scaling relations. Thus obtained value of the anomalous Hall conductivity (AHC) is found to be of the same order as the theoretically predicted value.[16] Since, intrinsic AHE is one of the characteristics of Weyl semimetals,[33,34] hence, the dominating intrinsic AHE in epitaxial Co_2MnGe thin film indicates the presence of a non-negligible Berry curvature in its electronic structure. Further experiments, such as ARPES on the epitaxially grown films of the Co_2MnGe, will be required to affirm the same. Nevertheless, our results from transport measurements provide further linkages for the Co_2MnGe Heusler alloy to be categorized as a Weyl semimetal.

2. Experimental details

Co_2MnGe thin films were grown on (100)-oriented MgO single crystal substrates using the PLD technique. Base pressure of $\sim 10^{-7}$ mbar was maintained in the deposition chamber inside which, a bulk target (Co: 50%, Mn: 25%, Ge: 25%) was continuously hit by pulsed laser light from an excimer KrF laser (Coherent Inc.) at 248 nm wavelength and variable repetition rate and energy. The laser beam was incident on the target at a 45° incident angle to avoid any plume disorientation. To ensure film homogeneity, the target surface was continuously rotated and toggled at a fixed distance ($\sim$4 cm) below the substrate. Vacuum environment of $\sim 10^{-6}$ mbar was maintained during the deposition process. A range of the growth temperatures, the laser fluences and the laser repetition rates were implemented for the initial optimization process. The optimized growth conditions for epitaxial thin films were with the growth temperature of 773 K, laser fluence of 2.6 J cm^{-2} and pulse repetition rate of 7 Hz. An *in situ* post-annealing was conducted at the same temperature for 1 hour to further enhance the crystallinity and chemical ordering.

An X-ray diffractometer (PANalytical X'Pert) having Cu-Kα radiation source (λ = 1.5406 Å) was used for analyzing crystal structure and crystalline quality of the Co_2MnGe films. ϕ-scan measurements helped to confirm the epitaxial quality of the films while thickness, density, and surface roughness for the film were determined from X-ray reflectivity (XRR) data. Elemental composition of the Co_2MnGe film was determined by using electron probe microanalysis (EPMA) as described in the ESI Section S2.† An atomic force microscope (AFM by Asylum Research) was used to investigate the films' surface morphology at room temperature. Magnetization measurements were performed using a magnetic property measurement system (MPMS by Quantum Design, USA). Transport measurements for longitudinal resistivity, magnetoresistance, and AHE were carried out by using a physical property measurement system (PPMS by Quantum Design, USA).

3. Results and discussion

3.1. Structural analysis

The XRD pattern at room temperature is shown in Fig. 1(a). For a comparison, the data for the bare substrate is also presented. The presence of (200) and (400) reflections at $2\theta = 31.34°$ and 65.3°, respectively, indicates formation of an epitaxial Co_2MnGe film with a B2-type structure oriented along (100) direction of the substrate. The absence of any extra peaks is strong evidence of the phase purity of the thin film sample. From these results, we determine the value of the lattice constant to be a_{Co_2MnGe} = 5.71 Å, which is in good agreement with the literature.[35,36] We estimate mean size of the highly oriented crystallites in the plane of the film to be $\sim$15 nm from the Scherrer's formula, $D = [0.9\lambda/\beta \cos\theta]$, where β is the full width at half-maximum of the diffraction peak, λ is the X-ray wavelength in nm, and θ is the diffraction angle in degrees. Results from ϕ-scan measurements carried out along the (220) plane ($2\theta = 45.3°$ and $\chi = 45°$) of the Co_2MnGe film and along the (220) plane ($2\theta = 62.3°$ and $\chi = 45°$) of the MgO substrate, are shown in Fig. 1(b). Four well-defined peaks, periodically separated from one another with an angular difference of 90°, clearly demonstrate an underlying fourfold crystalline symmetry. To substantiate the epitaxial growth of the Co_2MnGe film on the MgO(100) substrate, we also recorded ϕ-scans along the (111) planes ($2\theta = 27.3°$ and $\chi = 54.7°$) in which no reflections were observed. From all the above, it can be concluded that (100)-oriented Co_2MnGe epitaxial thin film with B2-type crystalline ordering was grown by PLD.

As inferred from the X-ray analysis in the above paragraph, schematic unit cell structure is shown in Fig. 1(c) in which, the crystallographic orientations of Co_2MnGe on the MgO substrate are also indicated. In the figure, the picture on the left represents unit cell of the B2-ordered Co_2MnGe crystal, where antisite disorder is present at Mn and Ge positions, while the image on the right is the top-view showing the Co_2MnGe unit cell, positioned diagonally on the MgO substrate. The XRR data for the thin film is presented in Fig. 1(d), where the solid red curve is the best fit obtained by following recursive Parratt formalism.[37] From the fitting, we obtain the film thickness of 45 $\pm$ 1.5 nm and roughness of 3 $\pm$ 0.3 nm. The relatively high roughness here can be attributed to the large grain size, as evidenced from the AFM image of the film. The same is presented as inset in Fig. 1(d), from which we estimate an average grain size of $\sim$180 nm. From the AFM image, the root mean square roughness is estimated to be $\sim$3.2 nm, a value consistent with the result obtained from the XRR analysis.

3.2. Magnetization, electrical resistivity, and magnetoresistance

A soft ferromagnetic behavior with coercivity value of 140 Oe at 300 K is evident from the *M–H* curves recorded at different

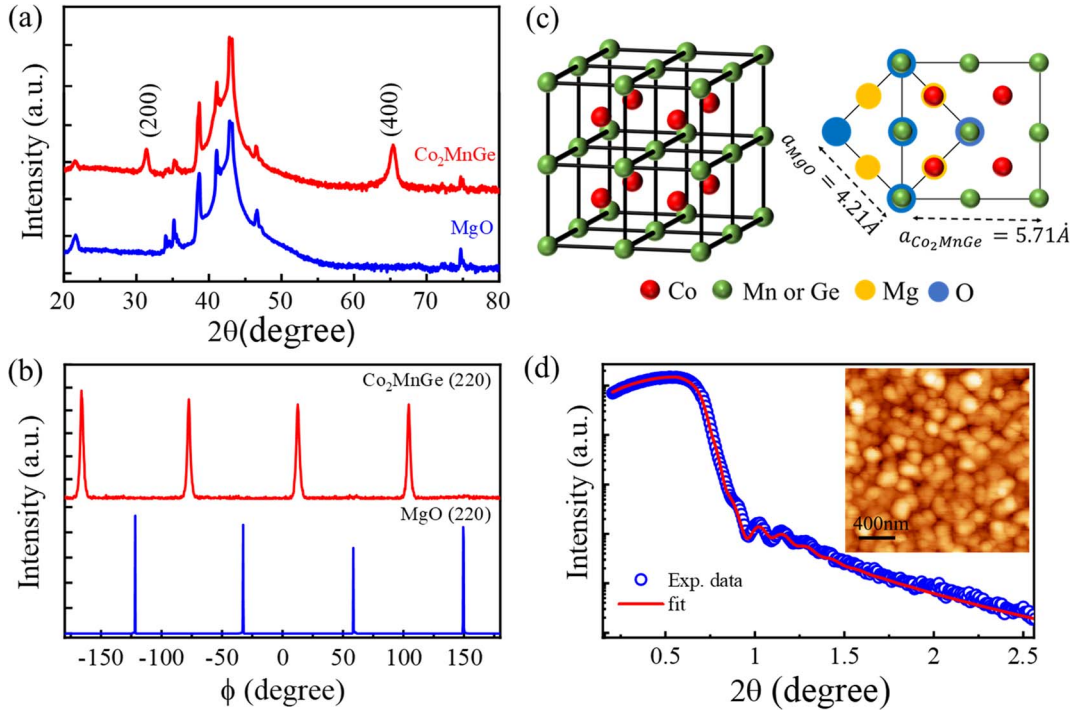

Fig. 1 Crystal structure and surface morphology of PLD grown (100)-oriented epitaxial Co_2MnGe thin film on MgO(100) substrate. (a) Out-of-plane XRD patterns and (b) ϕ-scan data (along (220) planes) of the Co_2MnGe film (top) and the MgO substrate (bottom). (c) Schematic of the B2-ordered crystal structure (left) and top view of Co_2MnGe unit cell over MgO lattice (right). (d) X-ray reflectivity data (blue circles) and fit (red line) for the 45 nm thick Co_2MnGe film. Inset: AFM image (2 × 2 μm^2) with a scale bar of 400 nm.

sample temperatures as shown in Fig. 2(a). We estimate the value of the saturation magnetization to be $M_s \sim 2.7\mu_B$ f.u.$^{-1}$ at 300 K and $M_s \sim 3.4\mu_B$ f.u.$^{-1}$ at 50 K. These values are smaller than those reported in the literature for L21-phase Co_2MnGe.[32,38] Indeed, the smaller value of the saturation moment in the present case is consistent with the reduced chemical ordering in the B2-phase Co_2MnGe.[30,38] Fig. 2(b) shows the variation of M_s with sample temperature. A slight increment in M_s with the decreasing temperature can be attributed to the pinning of magnetic moments at low temperatures.

Fig. 2(c) illustrates the behavior of the longitudinal resistivity (ρ_{xx}) *vs.* sample temperature (2–300 K) in the absence of any external magnetic field. The experimentally measured resistivity-temperature curve shows metallic nature of the epitaxial Co_2MnGe film. A minimum in the resistivity in the vicinity of 25 K is followed by an upturn as the temperature decreases further. Such type of low-temperature anomaly in the resistivity can be attributed to the disorder-enhanced coherent backscattering of conduction electrons due to weak localization.[28,39] The residual resistivity near the lowest temperature of 2 K, due to scattering from the impurities and structural imperfections, is $\rho_{xx,0} \sim 160$ μΩ cm. From this result, we obtain residual resistivity ratio [RRR = ρ_{xx}(300 K)/ρ_{xx}(2 K)] of about 1.2, a value close to the previously reported ones for epitaxial thin films of different Co-based full Heusler alloys.[12,39,40]

Owing to the spin polarization of conduction electrons at the Fermi energy for one spin channel in half-metallic Heusler alloys, the spin flipping related single magnon scattering is prohibited at low temperatures. The possible scattering mechanisms to affect the temperature-dependent resistivity of a ferromagnet are (a) electron–electron scattering (T^2-dependence), (b) electron–phonon scattering (T-dependence), and (c) double magnon scattering ($T^{9/2}$-dependence at low temperatures and $T^{7/2}$-dependence at higher temperatures).[41] In addition, scattering from disorders is accounted for by a $T^{1/2}$-dependent term. A careful observation of the experimental data in Fig. 2(c) necessitates fitting in two temperature regions, identified as region-I and region-II that are separated by a demarcation dashed line drawn at temperature of ∼80 K. The continuous curves in Fig. 2(c) are fittings to the data obtained as follows.

The best theoretical fit to the resistivity data in region-I (2–80 K) is obtained by using a relation, $\rho_{xx} = \rho_{xx,0} - AT^{1/2} + BT^2 + CT^{9/2}$. Here $\rho_{xx,0}$ represents the residual resistivity, while the coefficients A, B, and C represent the strengths of the weak localization, electron–electron, and double magnon scattering processes, respectively. Similarly, the best fit to the data in region-II (80–300 K) is obtained by using a relation, $\rho_{xx} = \rho_{xx,0} + DT + ET^2 + FT^{7/2}$, where the coefficients D, E and F represent the electron–phonon scattering, electron-magnon scattering and double magnon scattering strengths, respectively. At higher temperatures (region-II), it is imperative to add electron-magnon scattering term to obtain the best fit to the data. Therefore, unlike the case at low-temperatures (region-I), the single magnon scattering becomes viable at high temperatures (region-II) in half-metallic Heusler alloys.[42] Moreover, we find

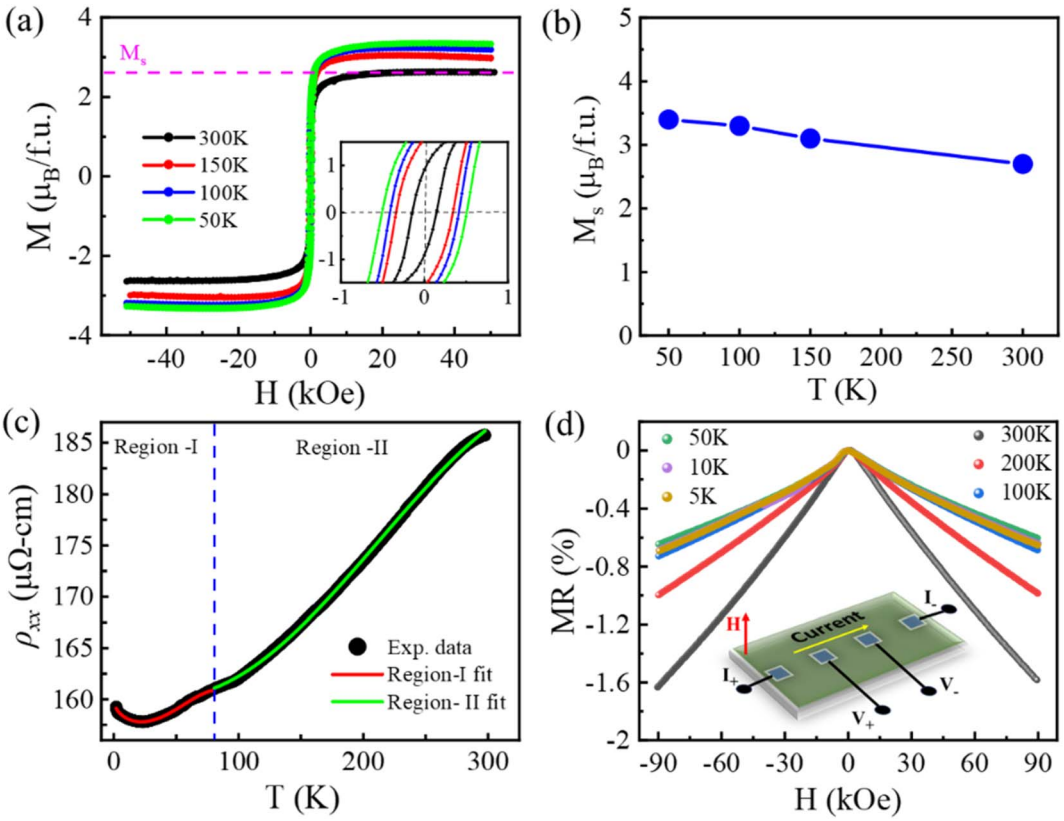

Fig. 2 Magnetic and electrical properties of the epitaxial Co_2MnGe film on MgO(100) substrate. (a) In-plane magnetic hysteresis (M–H) loops at various sample temperatures, plotted after subtracting the diamagnetic contribution of the MgO substrate. The zoomed-in-view in the inset is for determining the coercivity. (b) Variation of saturation magnetization (M_s) with the sample temperature. (c) Temperature-dependent (2–300 K) longitudinal resistivity and model fitting of the data in two distinct regions: low-T region of 2–80 K (region-I) and high-T region of 80–300 K (region-II). (d) Magnetoresistance data taken at different temperatures by varying the magnetic field perpendicular to the applied current. Inset: Schematic of the sample and measurement geometry.

that below a certain temperature in region-I, the A-term of ρ_{xx} due to weak localization dominates over others before the electron–electron scattering catches up with the increasing temperature. This leads to dip-like shape in region-I of the resistivity-temperature curve. On the other hand, in region-II, the D-term of ρ_{xx} due to electron–phonon scattering is dominant over the other processes. Double magnon scattering contributes to the $T^{9/2}$-dependence at low temperatures (region-I) and $T^{7/2}$-dependence at higher temperatures (region-II).[43] Therefore, half-metallic nature of the Co_2MnGe epitaxial film is evidenced from the resistivity-temperature data in the entire range of 2–300 K.

Results for the magnetoresistance (MR) of the Co_2MnGe epitaxial film are obtained by sweeping out-of-plane magnetic field from $H = -90$ kOe to +90 kOe. The same recorded at different sample temperatures are presented in Fig. 2(d). The linear four-probe geometry used for these measurements is also shown schematically in the inset of the figure. The MR in percentage is defined as $\text{MR}\ (\%) = \frac{[R(H) - R(0)]}{R(0)} \times 100$, where $R(0)$ is the resistance of the film at $H = 0$ kOe. It can be seen from the figure that the MR value is quite small and negative at all the investigated temperatures, from the lowest of 5 K to the highest of the room temperature. The above seems a usual behavior of the MR in different ferromagnetic Heusler alloys.[19,44]

3.3. Anomalous Hall effect

Dominating intrinsic AHE in epitaxial Co_2MnGe thin films is established here from detailed magnetotransport measurements performed over a temperature range of 5–300 K. The results for experimentally measured Hall resistivity ρ_{xy} are presented in Fig. 3(a) for different sample temperatures in the entire range. For these measurements, a rectangular piece of the sample having dimensions of 5 mm × 3 mm was utilized on which electrical contacts were made in the Hall geometry, as shown schematically in the inset of Fig. 3(a). Contributions from voltage probe misalignment are avoided by averaging for opposite fields in the form, $\rho_{xy}(H) = \frac{[\rho_{xy}(+H) - \rho_{xy}(-H)]}{2}$. The magnetic field was swept from $H = -90$ kOe to +90 kOe and measurements were repeated at different temperatures. A minimal dc charge current of 100 μA was used in these experiments. As can be seen from Fig. 3(a), the Hall resistivity initially increases sharply up to a field of ~10 kOe, before the slope of the curves changes drastically. Therefore, two regions in the

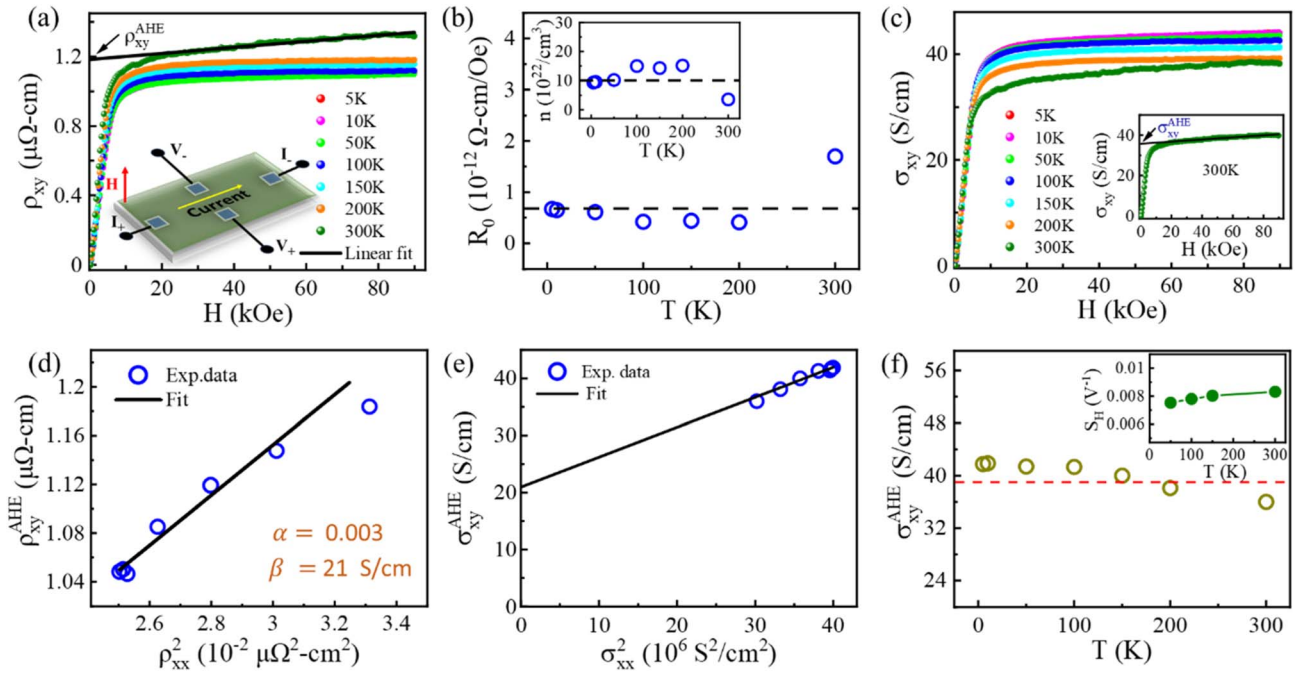

Fig. 3 AHE in epitaxial Co_2MnGe thin film. (a) Magnetic field-dependent Hall resistivity, ρ_{xy} at various sample temperatures as indicated. The solid line represents linear fit to the data at high field values and extrapolated to zero field to infer the anomalous Hall resistivity, ρ_{xy}^{AHE}. Inset: experimental geometry adopted for these measurements. (b) Ordinary Hall coefficient as a function of the sample temperature. Inset: calculated values of the carrier concentration. (c) Field-dependent Hall conductivity at various temperatures. Inset represents the linear fitting of the data at high fields and extrapolated to zero field to infer the anomalous Hall conductivity, σ_{xy}^{AHE}. (d) Variation of ρ_{xy}^{AHE} with ρ_{xx}^2, and (e) variation of σ_{xy}^{AHE} with σ_{xx}^2. Solid lines are fits obtained using the TYJ model as discussed in the text. (f) Temperature-dependence of σ_{xy}^{AHE}. Inset: temperature-dependence of scaling coefficient, S_H.

Hall resistivity curves can be clearly distinguished. Such a behaviour of total ρ_{xy} in a ferromagnetic system can be expressed in terms of an ordinary Hall resistivity, ρ_{xy}^{OHE} and anomalous Hall resistivity, ρ_{xy}^{AHE}, *via* the following relation[20,45]

$$\rho_{xy} = \rho_{xy}^{OHE} + \rho_{xy}^{AHE} = R_0 H + 4\pi R_S M \quad (1)$$

Here, R_0 and R_s are the ordinary and anomalous Hall coefficients, respectively, for the applied magnetic field H and spontaneous magnetization M in the material. The ρ_{xy}^{OHE} pitches in at the high-field region, above 10 kOe, where the overall ρ_{xy} shows a very weak linear field-dependence, up to 90 kOe. The values of ρ_{xy}^{AHE} and R_0 can be obtained from a linear fit to the ρ_{xy} *vs.* H curves in the high-field region (>10 kOe) using eqn (1), for which, one representative fit is shown in Fig. 3(a) for the sample temperature of 300 K. The y-axis intercept and the slope of the linear fit correspond to ρ_{xy}^{AHE} and R_0, respectively, while the anomalous Hall coefficient R_S is calculated from the relation $\rho_{xy}^{AHE} = 4\pi R_S M$ (see ESI Section S1†).

Fig. 3(b) displays the values of R_0 at all temperatures obtained by the fitting procedure as discussed above. Positive values of R_0 indicate that holes are majority charge carriers in the whole temperature range. Using the relation, $n = 1/R_0 e$, where e is electronic charge, we have also calculated the hole concentration n in the film at different temperatures as shown in the inset of Fig. 3(b). The mean value of the hole concentration in the film at all temperatures is $n \sim 10^{22}$ to 10^{23} cm^{-3}, which is sufficiently large to provide metal-like behaviour in the electrical resistivity, as discussed earlier.

Magnetic field-dependent Hall conductivity, $\sigma_{xy}(H)$ can be obtained by using the relation[46]

$$\sigma_{xy}(H) = \frac{\rho_{xy}(H)}{\rho_{xx}^2(H=0) + \rho_{xy}^2(H)}, \quad (2)$$

and the corresponding results are presented in Fig. 3(c) for all the sample temperatures in the experiments. The inset in the figure is drawn to explicitly show the value of the AHC, σ_{xy}^{AHE} at a given sample temperature obtained by fitting the data at high field values with a linear curve and extrapolating it to the zero-field axis. At the room temperature, we determine $\sigma_{xy}^{AHE} \sim 36$ S cm^{-1}, a value in the same order as that reported from theoretical calculations for an ideal Co_2MnGe model system.[16]

The temperature dependent anomalous Hall resistivity is now analysed here. We first plot the ρ_{xy}^{AHE} as a function of the squared longitudinal resistivity, ρ_{xx}^2 at the varying sample temperatures, as shown in Fig. 3(d). To extract the contributions from the intrinsic and extrinsic mechanisms in the AHE, a scaling relation as proposed by Tian *et al.*[25] and popularly known as the TYJ model is used, according to which,

$$\rho_{xy}^{AHE}(T) = \alpha \rho_{xx,0} + \beta \rho_{xx}^2(T) \quad (3)$$

Here, parameter α represents the extrinsic contribution depending on the residual longitudinal resistivity, while the parameter β represents intrinsic anomalous Hall conductivity,

$\sigma_{xy}^{AHE,in}$. It may be recalled from the discussion before that the intrinsic AHE is due to Berry curvature associated with the electronic band structure, while the extrinsic contribution arises from skew scattering and side jumps from disorders/impurities.[26] The continuous curve in Fig. 3(d) is fit obtained by using eqn (3) in conjunction with the values of $\rho_{xx,0}$ and ${\rho_{xx}}^2$ as obtained before, providing values of $\alpha \sim 0.003$ and $\beta = \sigma_{xy}^{AHE,in} \sim 21$ S cm^{-1}. The TYJ model has also been used in the literature directly in terms of AHC[25,47–49] as $\sigma_{xy}^{AHE}(T) = \alpha \frac{{\sigma_{xx}}^2(T)}{\sigma_{xx,0}} + \beta$, where $\sigma_{xx,0} = \frac{1}{\rho_{xx,0}}$, $\sigma_{xx}(T) = \frac{1}{\rho_{xx}(T)}$, and the intercept value β directly providing the numerical value of the intrinsic anomalous Hall conductivity. The corresponding result and linear fit are shown in Fig. 3(e) and the same value of $\sigma_{xy}^{AHE,in} \sim 21$ S cm^{-1} is obtained from it in the limit of $\sigma_{xx} \to 0$. By comparing thus obtained values of $\sigma_{xy}^{AHE,in}$ and overall σ_{xy}^{AHE} (300 K), we conclude that intrinsically dominated AHE occurs in epitaxial Co_2MnGe thin film in the current study. Furthermore, by following the procedure in eqn (2) and the results in Fig. 3(c) for each individual sample temperature, the values of σ_{xy}^{AHE} at all temperatures are plotted in Fig. 3(f). From such a representation[33,50] and the observation of nearly temperature independent σ_{xy}^{AHE}, we get further evidence of intrinsically dominating AHC. We note that almost same temperature-dependent behavior is shown by the saturation magnetization M_S in Fig. 2(b) and the anomalous Hall conductivity σ_{xy}^{AHE} in Fig. 3(f). Therefore, σ_{xy}^{AHE} is approximately proportional to M_S, indicating constant behaviour of the scaling coefficient, $S_H = \frac{R_S \mu_0}{{\rho_{xx}}^2} = \frac{\sigma_{xy}^{AHE}}{M_S}$ with respect to the temperature. Here, μ_0 is the vacuum permeability. The same can be evidenced from our results as shown in the inset of Fig. 3(f), thereby, confirming the dominating intrinsic contribution to AHC.[29,51]

4. Conclusions

To summarize, we have synthesized epitaxial thin films of ferromagnetic Co_2MnGe Heusler alloy on MgO(100) substrate by using PLD under optimized growth conditions. Structural and morphological investigations have revealed uniformly oriented large-size grains in B2-phase. An in-plane saturation magnetization value of $\sim 3.4 \mu_B$ f.u.$^{-1}$ at 50 K, and $\sim 2.7 \mu_B$ f.u.$^{-1}$ at 300 K was measured for the above metallic thin film whose longitudinal electrical resistivity is minimum around temperature of $\sim$25 K due to the presence of a weak localization effect. An expanded scaling mechanism has been performed to analyze the experimentally measured anomalous Hall resistivity, which confirms a dominating intrinsic origin of AHE in the epitaxial Co_2MnGe thin film.

Author contributions

SK supervised the work. EY performed the experiments. SK and EY analyzed the results and wrote the manuscript.

Conflicts of interest

The authors declare no conflict of interests.

Acknowledgements

SK acknowledges the Science and Engineering Research Board (SERB), Department of Science and Technology, Government of India, for financial support through Project No. CRG/2020/000892. Joint Advanced Technology Center, IIT Delhi is also acknowledged for support through EMDTERA#5 project. EY acknowledges the University Grant Commission, Government of India, for Senior Research Fellowship. We acknowledge the Central Research Facility, IIT Delhi for PPMS measurements, and the Physics Department, IIT Delhi for PLD, MPMS, AFM and XRD facilities.

References

1 F. Heusler, *Verh. Dtsch. Phys. Ges.*, 1903, **5**, 219.
2 I. Galanakis, P. H. Dederichs and N. Papanikolaou, *Phys. Rev. B: Condens. Matter Mater. Phys.*, 2002, **66**, 174429.
3 I. Belopolski, K. Manna, D. S. Sanchez, G. Chang, B. Ernst, J. Yin, S. S. Zhang, T. Cochran, N. Shumiya, H. Zheng, B. Singh, G. Bian, D. Multer, M. Litskevich, X. Zhou, S.-M. Huang, B. Wang, T.-R. Chang, S.-Y. Xu, A. Bansil, C. Felser, H. Lin and M. Z. Hasan, *Science*, 2019, **365**, 1278–1281.
4 J. Goraus, J. Czerniewski, K. Prusik and M. Fijałkowski, *J. Alloys Compd.*, 2021, **867**, 159078.
5 T. Graf, C. Felser and S. S. P. Parkin, *Prog. Solid State Chem.*, 2011, **39**, 1–50.
6 H. C. Kandpal, G. H. Fecher and C. Felser, *J. Phys. D: Appl. Phys.*, 2007, **40**, 1507.
7 J. Kübler, G. H. Fecher and C. Felser, *Phys. Rev. B: Condens. Matter Mater. Phys.*, 2007, **76**, 024414.
8 R. A. de Groot, F. M. Mueller, P. G. v. Engen and K. H. J. Buschow, *Phys. Rev. Lett.*, 1983, **50**, 2024–2027.
9 T. Kono, M. Kakoki, T. Yoshikawa, X. Wang, K. Goto, T. Muro, R. Y. Umetsu and A. Kimura, *Phys. Rev. Lett.*, 2020, **125**, 216403.
10 S. Picozzi, A. Continenza and A. J. Freeman, *Phys. Rev. B: Condens. Matter Mater. Phys.*, 2004, **69**, 094423.
11 T. Taira, T. Ishikawa, N. Itabashi, K.-i. Matsuda, T. Uemura and M. Yamamoto, *Appl. Phys. Lett.*, 2009, **94**, 072510.
12 T. Ambrose, J. J. Krebs and G. A. Prinz, *Appl. Phys. Lett.*, 2000, **76**, 3280–3282.
13 D. Asakura, T. Koide, S. Yamamoto, K. Tsuchiya, T. Shioya, K. Amemiya, V. R. Singh, T. Kataoka, Y. Yamazaki, Y. Sakamoto, A. Fujimori, T. Taira and M. Yamamoto, *Phys. Rev. B: Condens. Matter Mater. Phys.*, 2010, **82**, 184419.
14 K. Gross, P. Szary, O. Petracic, F. Brüssing, K. Westerholt and H. Zabel, *Phys. Rev. B: Condens. Matter Mater. Phys.*, 2011, **84**, 054456.
15 S. Jena, M. Zzaman, V. K. Verma, K. Ishigami, G. Shibata, T. Ishikawa, G. f. Li, M. Yamamoto, R. Shahid, T. Koide, A. Fujimori and V. R. Singh, *Phys. B*, 2022, **627**, 413619.

16 A. Sharan, F. Crasto de Lima, S. Khalid, R. H. Miwa and A. Janotti, *Phys. Status Solidi - Rapid Res. Lett.*, 2022, **16**, 2100652.
17 M. Hirschberger, S. Kushwaha, Z. Wang, Q. Gibson, S. Liang, C. A. Belvin, B. A. Bernevig, R. J. Cava and N. P. Ong, *Nat. Mater.*, 2016, **15**, 1161–1165.
18 T. Suzuki, R. Chisnell, A. Devarakonda, Y. T. Liu, W. Feng, D. Xiao, J. W. Lynn and J. G. Checkelsky, *Nat. Phys.*, 2016, **12**, 1119–1123.
19 K. Manna, L. Muechler, T.-H. Kao, R. Stinshoff, Y. Zhang, J. Gooth, N. Kumar, G. Kreiner, K. Koepernik, R. Car, J. Kübler, G. H. Fecher, C. Shekhar, Y. Sun and C. Felser, *Phys. Rev. X*, 2018, **8**, 041045.
20 N. Nagaosa, J. Sinova, S. Onoda, A. H. MacDonald and N. P. Ong, *Rev. Mod. Phys.*, 2010, **82**, 1539–1592.
21 R. Karplus and J. M. Luttinger, *Phys. Rev.*, 1954, **95**, 1154–1160.
22 S. Onoda, N. Sugimoto and N. Nagaosa, *Phys. Rev. B: Condens. Matter Mater. Phys.*, 2008, **77**, 165103.
23 R. Takahashi and N. Nagaosa, *Phys. Rev. B*, 2015, **91**, 245133.
24 D. Xiao, M.-C. Chang and Q. Niu, *Rev. Mod. Phys.*, 2010, **82**, 1959–2007.
25 Y. Tian, L. Ye and X. Jin, *Phys. Rev. Lett.*, 2009, **103**, 087206.
26 L. Wu, K. Zhu, D. Yue, Y. Tian and X. Jin, *Phys. Rev. B*, 2016, **93**, 214418.
27 Y. Zhang, Y. Yin, G. Dubuis, T. Butler, N. V. Medhekar and S. Granville, *npj Quantum Mater.*, 2021, **6**, 17.
28 S. Husain, A. Kumar, S. Akansel, P. Svedlindh and S. Chaudhary, *J. Magn. Magn. Mater.*, 2017, **442**, 288–294.
29 S. Roy, R. Singha, A. Ghosh, A. Pariari and P. Mandal, *Phys. Rev. B*, 2020, **102**, 085147.
30 M. Obaida, K. Westerholt and H. Zabel, *Phys. Rev. B: Condens. Matter Mater. Phys.*, 2011, **84**, 184416.
31 T. Ishikawa, T. Marukame, K.-i. Matsuda, T. Uemura, M. Arita and M. Yamamoto, *J. Appl. Phys.*, 2006, **99**, 08J110.
32 M. Yamamoto, T. Marukame, T. Ishikawa, K. Matsuda, T. Uemura and M. Arita, *J. Phys. D: Appl. Phys.*, 2006, **39**, 824–833.
33 Q. Wang, Y. Xu, R. Lou, Z. Liu, M. Li, Y. Huang, D. Shen, H. Weng, S. Wang and H. Lei, *Nat. Commun.*, 2018, **9**, 3681.
34 K. Manna, Y. Sun, L. Muechler, J. Kübler and C. Felser, *Nat. Rev. Mater.*, 2018, **3**, 244–256.
35 M. Özduran, A. Candan, S. Akbudak, A. K. Kushwaha and A. İyigör, *J. Alloys Compd.*, 2020, **845**, 155499.
36 S. Ishida, S. Fujii, S. Kashiwagi and S. Asano, *J. Phys. Soc. Jpn.*, 1995, **64**, 2152–2157.
37 L. G. Parratt, *Phys. Rev.*, 1954, **95**, 359–369.
38 A. Rajanikanth, Y. K. Takahashi and K. Hono, *J. Appl. Phys.*, 2007, **101**, 023901.
39 Q. Wang, Z. Wen, T. Kubota, T. Seki and K. Takanashi, *Appl. Phys. Lett.*, 2019, **115**, 252401.
40 A. Markou, D. Kriegner, J. Gayles, L. Zhang, Y.-C. Chen, B. Ernst, Y.-H. Lai, W. Schnelle, Y.-H. Chu, Y. Sun and C. Felser, *Phys. Rev. B*, 2019, **100**, 054422.
41 L. Bainsla, K. G. Suresh, A. K. Nigam, M. Manivel Raja, B. S. D. C. S. Varaprasad, Y. K. Takahashi and K. Hono, *J. Appl. Phys.*, 2014, **116**, 203902.
42 C. G. F. Blum, C. A. Jenkins, J. Barth, C. Felser, S. Wurmehl, G. Friemel, C. Hess, G. Behr, B. Büchner, A. Reller, S. Riegg, S. G. Ebbinghaus, T. Ellis, P. J. Jacobs, J. T. Kohlhepp and H. J. M. Swagten, *Appl. Phys. Lett.*, 2009, **95**, 161903.
43 S. Chatterjee, J. Sau, S. Samanta, B. Ghosh, N. Kumar, M. Kumar and K. Mandal, *Phys. Rev. B*, 2023, **107**, 125138.
44 D. Zhang, Z. Hou and W. Mi, *Appl. Phys. Lett.*, 2022, **120**, 232401.
45 M. S. Gabor, M. Belmeguenai, T. Petrisor, C. Ulhaq-Bouillet, S. Colis and C. Tiusan, *Phys. Rev. B*, 2015, **92**, 054433.
46 S. Tong, Z. Xupeng, D. Wei and J. Zhao, *Phys. Rev. B*, 2020, **101**, 184434.
47 K. I. A. Khan, R. S. Yadav, H. Banxgar, A. Kumar, N. Chowdhury, P. K. Muduli and P. K. Muduli, *Nanoscale*, 2022, **14**, 8484–8492.
48 L. Ye, M. Kang, J. Liu, F. von Cube, C. R. Wicker, T. Suzuki, C. Jozwiak, A. Bostwick, E. Rotenberg, D. C. Bell, L. Fu, R. Comin and J. G. Checkelsky, *Nature*, 2018, **555**, 638–642.
49 J. Shen, Q. Yao, Q. Zeng, H. Sun, X. Xi, G. Wu, W. Wang, B. Shen, Q. Liu and E. Liu, *Phys. Rev. Lett.*, 2020, **125**, 086602.
50 G. K. Shukla, J. Sau, N. Shahi, A. K. Singh, M. Kumar and S. Singh, *Phys. Rev. B*, 2021, **104**, 195108.
51 Q. Wang, S. Sun, X. Zhang, F. Pang and H. Lei, *Phys. Rev. B*, 2016, **94**, 075135.